

A Corkscrew Model for Highly Coupled Anisotropic Compliance in Ruddlesden–Popper Oxides with Frozen Octahedral Rotations

Chris Ablitt¹, Mark S. Senn^{*,2}, Nicholas C. Bristowe^{†,3}, and Arash A. Mostofi^{1,4}

¹Department of Materials, Imperial College London, London SW7 2AZ, U.K.

²Department of Chemistry, University of Warwick, Gibbet Hill, Coventry, CV4 7AL, U.K.

³School of Physical Sciences, University of Kent, Canterbury CT2 7NH, U.K.

⁴Department of Physics, Imperial College London, London SW7 2AZ, U.K.

March 11, 2021

Abstract

A “corkscrew” mechanism, that couples changes in the in-plane rotation angle to strains along the layering axis, has been proposed previously to explain increased compliance in certain Ruddlesden–Popper phases that facilitates uniaxial negative thermal expansion over a wide temperature range. Following the procedure developed to study many simple, auxetic geometries, in the present study we derive the elastic compliances predicted by this corkscrew mechanism assuming that the four shortest metal–anion bonds remain stiff and changes in bond angle are modelled by a harmonic angle potential. We subsequently analyse the limitations of this model and show that it may be extended to $A_{n+1}B_nO_{3n+1}$ Ruddlesden–Popper oxide phases of general layer thickness n .

1 Introduction

The study of *negative* material properties, such as *negative Poisson’s ratio* (NPR), *negative linear compressibility* (NLC) and *negative thermal expansion* (NTE), has become an exciting field in materials chemistry. These unusual properties defy conventional intuition regarding how materials should behave and as such much work has gone into developing mechanisms to explain their occurrence in the rare examples of materials in which these phenomena manifest. In many cases, especially in metal organic framework (MOF) and inorganic framework materials, these explanations have involved describing the structure using simple geometric models.

The *Acaa* phase of $\text{Ca}_3\text{Mn}_2\text{O}_7$ exhibits uniaxial negative thermal expansion over a wide temperature range of approximately 950 K – between when the NTE phase first coexists alongside a competing low temperature phase up until when the material decomposes [1]. This compound is a member of the Ruddlesden–Popper (RP) oxide series, a class of layered perovskite materials with general formula $A_{n+1}B_nO_{3n+1}$ where A and B are cations and n denotes the number of ABO_3 perovskite layers stacked along the c axis, with blocks of n ABO_3 layers separated by a single AO rock salt layer. This discovery of NTE accompanies observations of uniaxial NTE along the layering axis in the analogous $n = 1$ $I4_1/acd$ phase of Ca_2MnO_4 [2, 3], Sr_2RhO_4 [4, 5, 6] and Sr_2IrO_4 [4] where, as in $n = 2$ *Acaa* $\text{Ca}_3\text{Mn}_2\text{O}_7$, rotations of BO_6 octahedra about the layering axis are frozen into the structure. RP phases with frozen octahedral rotations about the layering

*E-mail address: m.senn@warwick.ac.uk

†E-mail address: n.c.bristowe@kent.ac.uk

axis (but no frozen octahedral tilts about an in-plane axis) will herein be referred to as rotation phases.

NTE is often explained in similar framework materials using the theory of rigid unit modes [7, 8], soft vibrations of approximately rigid polyhedral structural units that drive contraction with increased temperature. Although we linked the decrease in magnitude of uniaxial NTE as x increases in $\text{Ca}_{3-x}\text{Sr}_x\text{Mn}_2\text{O}_7$ with the hardening of low frequency tilts (with tilt axis lying in the layer plane) of octahedra in DFT calculations [9], in a computational study performed on $I4_1/acd$ Ca_2GeO_4 we showed that highly anisotropic compliance is an essential ingredient for anisotropic NTE in these materials, alongside the soft phonons that provide the dynamic driving force [3]. The thermodynamic formalism distinguishing the vibrational contributions to thermal expansion from elements of the elastic compliance tensor was first derived almost 100 years ago [10] and the idea that anisotropic thermal expansion could be caused by anisotropic compliance was discussed based on experimental measurements of simple elements 40 years later [11]. In more recent years, studies based on first principles calculations have also discussed phonons and compliance separately when explaining computed thermal expansion [12].

In order to answer the question “why is NTE often seen in Ruddlesden-Popper oxide phases with a frozen octahedral rotation and not in equivalent phases of ABO_3 perovskite?” we proposed an atomic mechanism to explain this compliance that operates at the layer interface of RP rotation phases [3]. Since neither RP and ABO_3 rotation phases have frozen octahedral tilts, it is likely that these modes will be active to provide a thermodynamic driving force for uniaxial NTE in both structures and therefore the difference in anisotropic compliance is a key factor distinguishing the likelihood of the two materials to exhibit uniaxial NTE. Assuming that in a rotation phase of A_2BO_4 , the four most stiff metal – oxygen bonds remain rigid (the two distinct intra-octahedral B–O bonds and the two shortest A–O bonds), it is possible to cooperatively expand the a and b in-plane lattice parameters and contract the c layering axis by changing only bond angles allowed by the symmetry operations of the phase. This mechanism has been illustrated in Figure 1a. We liken this mechanism to a *corkscrew* since, like a corkscrew being screwed into a cork, an in-plane rotation leads to a decrease in height of the combined object (Figure 1b). In the layering plane, the three-dimensional BO_6 corner-linked octahedra are viewed as two-dimensional squares and therefore it should be clear from Figure 1c that changing the rotation angle of these rigid squares leads to a change in the in-plane lattice parameter.

In this paper we analyse this *corkscrew* mechanism and derive the elastic compliance matrix predicted if these bonds do indeed remain stiff and the resistance to deformation comes from a harmonic potential on certain metal–oxygen–metal bond angles. This follows the method used to analyse similar geometric systems, often in the field of auxetic (NPR) materials, for example to study simple two-dimensional systems formed from corner connected squares [13], triangles [14], rhombi [15] or rectangles of different sizes [16] or even to study more complex three-dimensional systems [17] as the RP structure is. Although we do not expect idealised models of this kind to represent exactly real chemical systems, analysis of this kind can be useful to understand mechanisms that operate in a real material alongside other effects. This manuscript is intended to support our recently accepted publication [18] where we assess through first-principles calculations how the anisotropic compliance changes in RP compounds with changing layer thickness n .

2 Derivation

Figure 2a shows an $n = 1$ A_2BO_4 Ruddlesden-Popper compound with a frozen octahedral rotation about the layering axis. This structure is visualised in the conventional manner for perovskite based chemistries: BO_6 octahedra are displayed as polyhedra (grey) with O ions at the corner linkages (red) and A cations (green) sitting in the interstitial sites with no A–O chemical bonds shown. The structure depicted in Figure 2 has an octahedral rotation that is in-phase between equivalent periodic image cells along [001], placing the cell in the $Acam$ space-group symmetry. However, the mechanism described in this report would apply equally well to a phase in which the octahedral rotations were exactly out-of-phase between adjacent periodic cells.

Figures 2b and 2c depict cross-sections of the (001) and (1 $\bar{1}$ 0) planes that are highlighted in orange and blue respectively in Figure 2a. Atoms lying on these planes are shown with thick

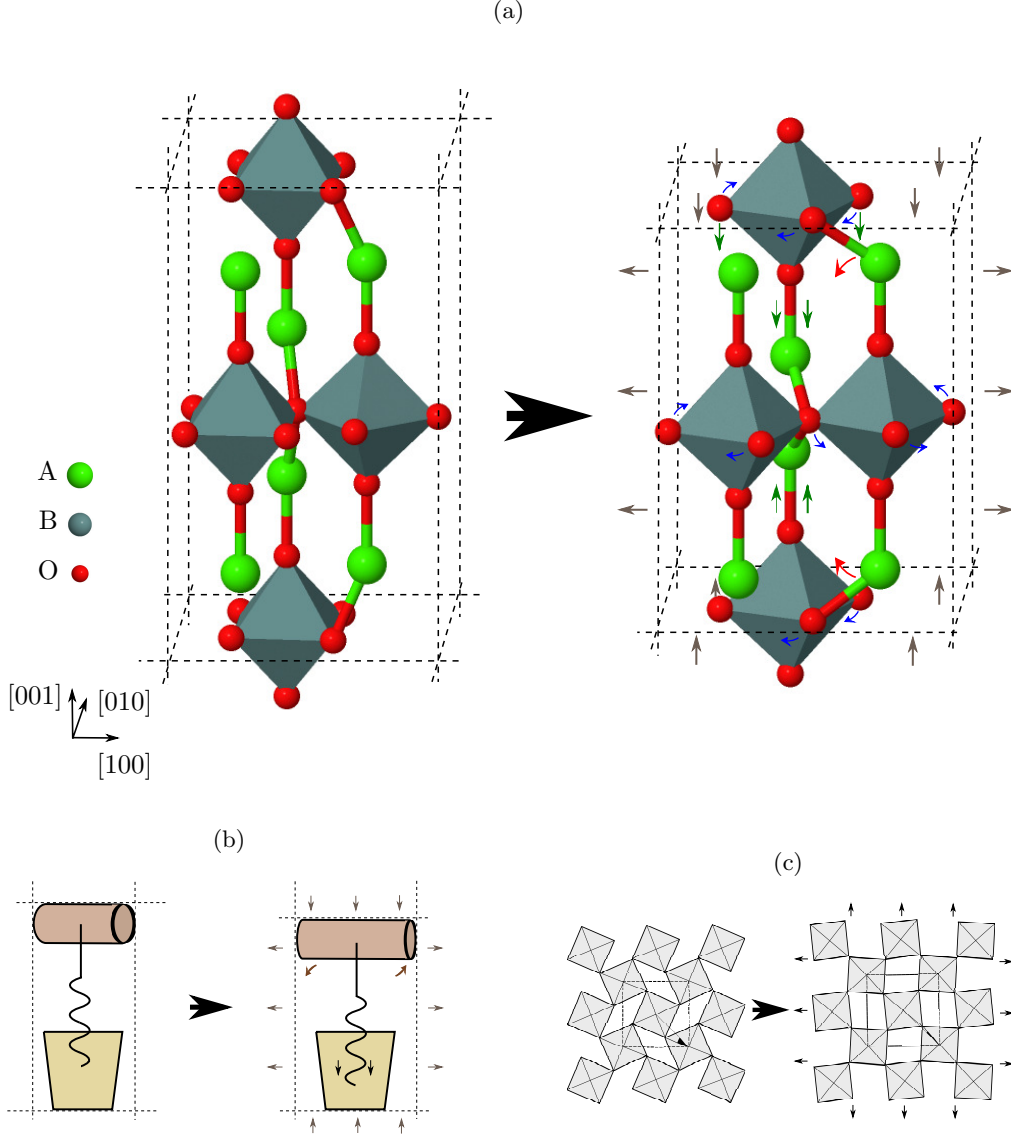


Figure 1: (a) The *corkscrew* mechanism in A_2BO_4 Ruddlesden–Popper oxides with a frozen rotation about the layering axis: a decrease in the in-plane rotation angle causes an in-plane expansion and a contraction along the layering axis; (b) a corkscrew being screwed into a cork: a change in the rotation angle also leads to an increase in the width of the two-dimensional picture but a decrease in the height of the combined object; and (c) the two-dimensional unit cell of rotated rigid corner-connected squares increases with a decrease in the rotation angle of each square.

dashed open circles and the shortest four metal-oxygen bonds that lie in these planes are shown as rigid struts. These four bonds consist of: the two distinct B–O bonds – between the central B cation and the equatorial (r_1) and apical oxygen (r_2) corner ions; the shortest A–O distance – across the AO layer interface between layers of adjacent BO_6 octahedra (r_3); and finally the shortest distance between the interface A cation and equatorial O anions (r_4). Equatorial O anions in the (001) plane do not actually lie in $(1\bar{1}0)$ due to the non-zero value of the rotation angle θ and in fact sit a distance of $r_1 \sin(\theta)$ from this plane. These O anions are shown as thick dotted open circles and the struts of length r_1 connecting these equatorial O ions to nearest neighbour B cations are shown projected onto $(1\bar{1}0)$.

The four shortest metal cation bonds ($r_1 - r_4$) were identified in our previous work to be the most stiff in DFT simulations on the $I4_1/acd$ phase of Ca_2GeO_4 [3]. In this work, we assume

$$\frac{\sqrt{2}X_1}{4} = r_4 \cos(\alpha) + r_1 \sin(\theta). \quad (4)$$

Combining Equations (2) and (4) leads to the relation

$$r_4 \cos(\alpha) = r_1 [\cos(\theta) - \sin(\theta)], \quad (5)$$

and therefore from Equation (5) we may compute the derivative, $\frac{d\alpha}{d\theta}$,

$$\frac{d\alpha}{d\theta} = \left(\frac{r_1}{r_4}\right) \left(\frac{\sin(\theta) + \cos(\theta)}{\sin(\alpha)}\right). \quad (6)$$

The Poisson's ratio, relating the strain of lattice parameter X_j to that of X_i is defined as

$$\nu_{ij} = -\frac{d\varepsilon_j}{d\varepsilon_i}, \quad (7)$$

where the incremental strain of X_i , $d\varepsilon_i$, is defined in terms of the incremental extension dX_i

$$d\varepsilon_i = \frac{dX_i}{X_i}. \quad (8)$$

Substituting Equation (2) into Equation (8), we may thus define the incremental strains of the X_1 and X_2 lattice parameters as

$$d\varepsilon_1 = d\varepsilon_2 = \frac{dX_1}{X_1} = \frac{1}{X_1} \frac{dX_1}{d\theta} d\theta = \frac{-2\sqrt{2}r_1 \sin(\theta)}{X_1} d\theta = -\tan(\theta) d\theta. \quad (9)$$

It is immediately apparent, since $d\varepsilon_1 = d\varepsilon_2$, that

$$\nu_{12} = \nu_{21} = -1. \quad (10)$$

This is the same result that was derived by Grima and Evans [19] for rigid squares on a 2D plane (recall Figure 1c), which is exactly what our system reduces to on the (001) cross-section shown in Figure 2b. In the present three-dimensional scheme, however, by substituting Equations (3) and (6) into Equation (8), we may also compute the incremental strain of the third lattice parameter, X_3 ,

$$\begin{aligned} d\varepsilon_3 = \frac{dX_3}{X_3} &= \frac{1}{X_3} \left(\frac{dX_3}{d\alpha}\right) \left(\frac{d\alpha}{d\theta}\right) d\theta = \frac{2r_4 \cos(\alpha)}{X_3} \left(\frac{r_1}{r_4}\right) \left(\frac{\sin(\theta) + \cos(\theta)}{\sin(\alpha)}\right) d\theta \\ &= \frac{2r_1}{X_3} \left(\frac{\sin(\theta) + \cos(\theta)}{\tan(\alpha)}\right) d\theta. \end{aligned} \quad (11)$$

It is therefore possible to compute the Poisson ratio, ν_{13} , relating $d\varepsilon_3$ to $d\varepsilon_1$,

$$\nu_{13} = -\frac{d\varepsilon_3}{d\varepsilon_1} = \left(\frac{X_1}{X_3}\right) \frac{2r_1 \left(\frac{\sin(\theta) + \cos(\theta)}{\tan(\alpha)}\right) d\theta}{2\sqrt{2}r_1 \sin(\theta) d\theta} = \left(\frac{X_1}{X_3}\right) \left(\frac{1 + \cot(\theta)}{\sqrt{2} \tan(\alpha)}\right), \quad (12)$$

and similarly for ν_{31} ,

$$\nu_{31} = -\frac{d\varepsilon_1}{d\varepsilon_3} = \frac{1}{\nu_{13}} = \left(\frac{X_3}{X_1}\right) \left(\frac{\sqrt{2} \tan(\alpha)}{1 + \cot(\theta)}\right). \quad (13)$$

In continuum elasticity, the strain energy, U , due to an incrementally small strain, $d\varepsilon_i$, is expressed in terms of the Young's modulus along i , E_i , as

$$U = 1/2 E_i (d\varepsilon_i)^2 = \frac{W}{V}. \quad (14)$$

In Equation (14), using the principle of conservation of energy, U has been equated to the work done by the cell, W , divided by the cell volume, V . In Equation (1), the work done per

hinge, w_φ is a quadratic function of the incremental change in hinge angle $d\varphi$ with stiffness k_φ , where φ is the hinge angle. By inspection of Figure 2b we see that the B–O–B θ -hinge angle is $\varphi_\theta = 180 - 2\theta$, so that $\frac{d\varphi_\theta}{d\theta} = -2$, and therefore the work done by a θ -hinge is

$$w_\theta = \frac{1}{2}k_\theta \left[\left(\frac{d\varphi_\theta}{d\theta} \right) d\theta \right]^2 = 2k_\theta (d\theta)^2. \quad (15)$$

Similarly, the A–O–A α -hinge angle is $\varphi_\alpha = 2\alpha$, so that we may express w_α as

$$w_\alpha = 2k_\alpha (d\alpha)^2. \quad (16)$$

If we define N_θ and N_α as the number of θ and α hinges respectively, we can express W as

$$W = 2 \left[N_\theta k_\theta (d\theta)^2 + N_\alpha k_\alpha (d\alpha)^2 \right]. \quad (17)$$

There are four θ -hinges per layer and for the $n = 1$ cell in Figure 2 there are two layers per unit cell, so $N_\theta = 8$. Similarly the $(\bar{1}10)$ cross section in Figure 2c shows two α -hinges, both bisected by the (002) plane (the middle BO_6 layer shown). The perpendicular cross section - the $(\bar{1}10)$ plane - also contains another two α hinges bisected by (002). Furthermore, there should be the same four α -hinges bisected by the (001) plane (the top BO_6 layer coloured in yellow in Figure 2c). By carefully studying Figure 2a it should be apparent that these four α -hinges bisected by (001) lie in the (220) and $(\bar{2}20)$ planes. Therefore $N_\alpha = N_\theta = 8$ and Equation (17) may be rewritten

$$W = 16 \left[k_\theta + k_\alpha \left(\frac{d\alpha}{d\theta} \right)^2 \right] (d\theta)^2. \quad (18)$$

Substituting Equation (18) into Equation (14), we may form the equation:

$$\frac{1}{2} E_i (d\varepsilon_i)^2 = \frac{16 \left[k_\theta + k_\alpha \left(\frac{d\alpha}{d\theta} \right)^2 \right] (d\theta)^2}{X_1^2 X_3}, \quad (19)$$

and substituting for $d\varepsilon_1$ from Equation (9),

$$\frac{1}{2} E_1 \left(\frac{8r_1^2 \sin^2(\theta) (d\theta)^2}{X_1^2} \right) = \frac{16 \left[k_\theta + k_\alpha \left(\frac{d\alpha}{d\theta} \right)^2 \right] (d\theta)^2}{X_1^2 X_3}, \quad (20)$$

we may form an expression for E_1

$$E_1 = \frac{4 \left[k_\theta + k_\alpha \left(\frac{d\alpha}{d\theta} \right)^2 \right]}{r_1^2 \sin^2(\theta) X_3}. \quad (21)$$

Similarly, substituting for $d\varepsilon_3$ from Equation (11), we find an expression for E_3 :

$$E_3 = \frac{8 \tan^2(\alpha) X_3 \left[k_\theta + k_\alpha \left(\frac{d\alpha}{d\theta} \right)^2 \right]}{r_1^2 [\sin(\theta) + \cos(\theta)]^2 X_1^2}. \quad (22)$$

The elastic compliance relates the strain experienced by a material to the applied stress. Expressing strain, ε_i , and stress, σ_j , as vectors in Voigt notation, we may define the elastic compliance matrix, s_{ij} , by the equation:

$$\varepsilon_i = s_{ij} \sigma_j \quad (23)$$

The mechanical model depicted in Figure 2 does not allow shearing, meaning that the ε_i ($i = 4, 5, 6$) terms will always be 0. Therefore we may restrict our strain/stress vectors to the first three terms in Voigt notation (the normal strains/stresses), making s_{ij} a 3×3 matrix with

all other components 0. In terms of the Young's moduli and Poisson ratios, s_{ij} may be expressed in general terms for an orthorhombic system with no strains:

$$\mathbf{s} = \begin{pmatrix} \frac{1}{E_1} & \frac{-\nu_{21}}{E_2} & \frac{-\nu_{31}}{E_3} \\ \frac{-\nu_{12}}{E_1} & \frac{1}{E_2} & \frac{-\nu_{32}}{E_3} \\ \frac{-\nu_{13}}{E_1} & \frac{-\nu_{23}}{E_2} & \frac{1}{E_3} \end{pmatrix} \quad (24)$$

And thus for our current system, in terms of the Young's moduli and Poisson ratios already derived, this becomes:

$$\mathbf{s} = \begin{pmatrix} \frac{1}{E_1} & \frac{1}{E_1} & \frac{-\nu_{31}}{E_3} \\ \frac{1}{E_1} & \frac{1}{E_1} & \frac{-\nu_{31}}{E_3} \\ \frac{-\nu_{13}}{E_1} & \frac{-\nu_{13}}{E_1} & \frac{1}{E_3} \end{pmatrix} \quad (25)$$

Substituting the values of ν_{13} , ν_{31} , E_1 and E_3 from Equations (12), (13), (21) & (22) into Equation (25) gives the full compliance matrix. It is then possible to confirm that \mathbf{s} satisfies the correct symmetry by verifying that:

$$\frac{\nu_{13}}{E_1} = \frac{\nu_{31}}{E_3} \quad (26)$$

3 Structural Limitations

For given bond lengths $r_1 - r_4$, the model has a single degree of structural freedom, θ , from which all other structural parameters, such as X_1 , X_3 and α may be computed. Although they are not restricted to be equal by symmetry, for simplicity of this analysis let us imagine that the two B-O bond lengths are equal ($r_1 = r_2$) and the two shortest A-O bond lengths are also equal ($r_3 = r_4$), giving only two independent bond lengths r_1 and r_4 . Aside from limiting the parameter space, this assumption has little effect since in all equations in Section 2, r_2 and r_3 appear only as the combination $r_2 + r_3$ in the formula for X_3 in Equation (3).

In this section we explore the structural limitations of the model with changing θ and r_4/r_1 assuming that all values of r_1 and r_4 are possible and that there are no interactions between any atoms not connected by a stiff rod ($r_1 - r_4$ in Figure 2).

Figure 3a shows how the in-plane lattice parameter, X_1 , varies with θ between the extreme values of $\theta = 0^\circ$ (corresponding to an unrotated, high-symmetry parent phase) and $\theta = 45^\circ$ (where the square cross sections of the BO_6 octahedra in the (001) plane are perfectly packed). The atoms lying on the (001) plane, the same plane shown previously in Figure 1b, are illustrated for these extreme values of θ in Figure 3b alongside a structure with an intermediate θ value. X_1 is independent of the r_4/r_1 ratio and may decrease to $\frac{1}{\sqrt{2}}$ of its value in the unrotated structure by increasing θ .

Figure 4a then shows how the lattice parameter along the layering axis, X_3 , varies between $\theta = 0^\circ$ and $\theta = 45^\circ$. Again Figure 4c shows a subset the atoms lying on the (110) plane, where this subset is an extension of the inset of Figure 1c, for $\theta = 0^\circ, 45^\circ$ and an intermediate value. Since X_3 depends upon α , which is itself a function of θ and r_4/r_1 , contours in Figure 4a show different r_4/r_1 ratios.

It should be apparent from the $\theta = 0^\circ$ panel of Figure 4c that $r_4 \geq r_1$. The $\theta = 0^\circ$ value of α , α_0 , then depends on r_4/r_1 , where $\alpha = 0^\circ$ only if $\theta = 0^\circ$ and $r_4 = r_1$. In the $\theta = 45^\circ$ limit, $\alpha = 90^\circ$ always as the A-O (r_4) bond aligns with the [001] direction. The greatest change in X_3 over the range of θ occurs when $r_4 = r_1$ such that X_3 may extend to $1.5 X_3(\theta = 0^\circ)$, although the rate of change in X_3 with α is greatest for low α , where $\sin(\alpha)$ is approximately linear. The rate of change of X_3 with θ is even greater for low θ and low r_4/r_1 since Figure 4b shows that $\frac{d\alpha}{d\theta} \gg 1$. In contrast, a large r_4/r_1 ratio leads to a large α_0 , decreasing both the range of α as θ varies $0^\circ \rightarrow 45^\circ$ and the rate of change of X_3 with α at higher α values.

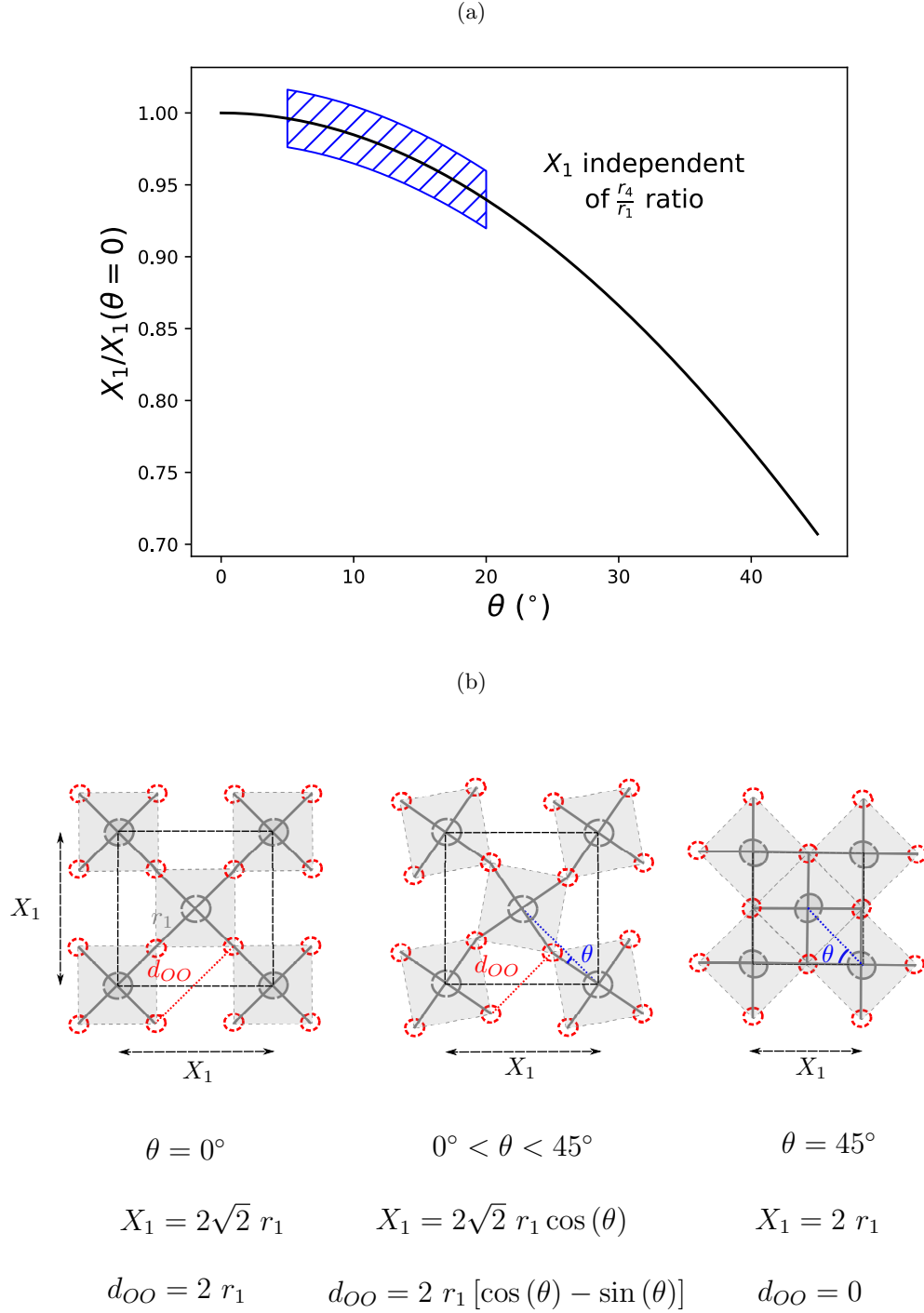


Figure 3: (a) The in-plane lattice parameter, X_1 , with changing θ in terms of X_1 when $\theta = 0^\circ$; (b) sketches of the (001)-plane cross section for different regimes of θ . The blue hashed region in (a) shows the range of θ where the mechanism may reasonably operate in a real system.

4 Physical Limitations

The previous section gave the maximum changes in X_1 and X_3 that may be achieved from varying θ over the range $[0^\circ, 45^\circ]$ and found that the greatest proportional change in X_3 is achieved when

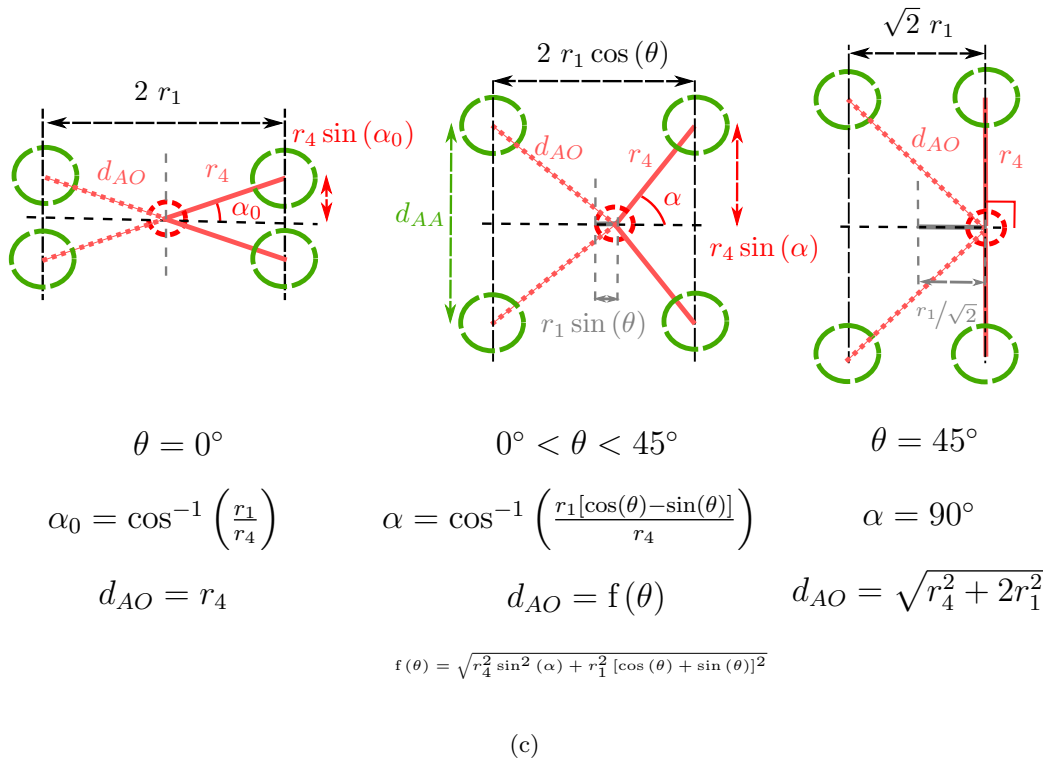
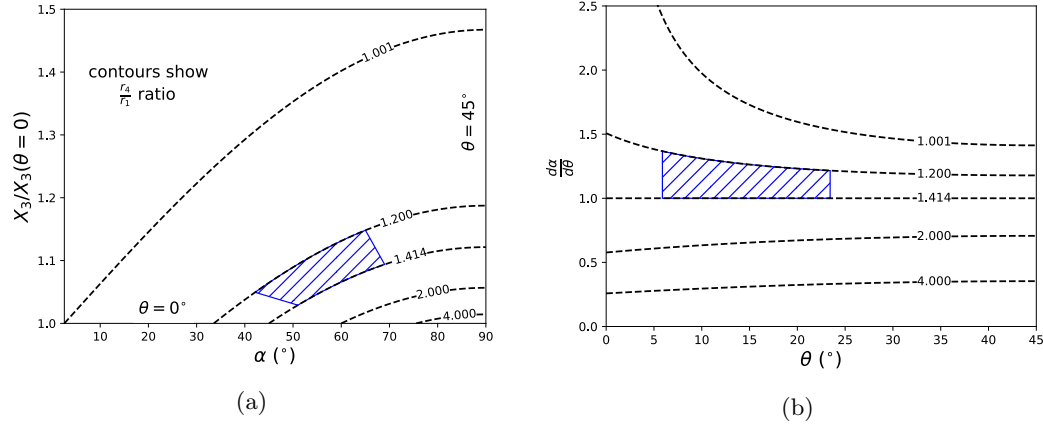


Figure 4: (a) The lattice parameter along the layering axis, X_3 , with changing α and r_4/r_1 as θ is varied between 0° and 45° ; (b) $\frac{d\alpha}{d\theta}$ as a function of θ for different r_4/r_1 ratios; (c) sketches of the $(1\bar{1}0)$ -plane cross section for different regimes of θ . The blue hashed regions in (a) & (b) show the ranges of θ and r_4/r_1 where the mechanism may reasonably operate in a real system.

$r_4 = r_1$. However, these limitations were extracted from the equations derived in Section 2 and did not consider whether the model could still be valid across the full range of θ and r_4/r_1 .

Figure 3b shows the shortest distance between equatorial O ions on neighbouring BO_6 octahedra, labelled d_{OO} . The corkscrew model does not consider these two O ions to interact. If $\theta = 0^\circ$, $d_{OO} = 2r_1$. However as θ increases, it can be seen from Figure 5 that d_{OO} becomes smaller until, in the limit $\theta = 45^\circ$, the two O ions lie on top of one another and thus $d_{OO} = 0$. This limit is clearly unphysical and one would expect that the two O ions should strongly repel one another at short distances. Therefore the assumption that the O ions have a negligible interaction is invalid at high θ . r_1 is the shortest *stiff* chemical bond in the system and even restricting that $d_{OO} > r_1$

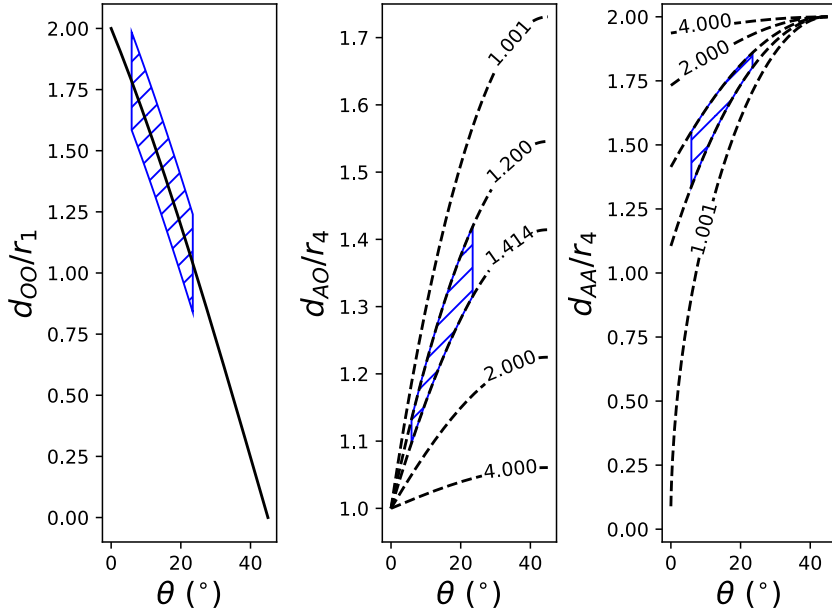


Figure 5: Interatomic distances d_{OO} , d_{AO} and d_{AA} , expressed in terms of fixed bond lengths r_1 or r_4 as a function of θ and r_4/r_1 . None of d_{OO} , d_{AO} and d_{AA} are restricted in the model, however the assumptions of the model become unreasonable if d_{OO} or d_{AA} become too small or if $d_{AO} \approx r_4$. Based on these criteria, the blue hashed region shows the ranges of θ and r_4/r_1 where the mechanism may reasonably operate in a real system.

imposes an upper limit of $\theta < 24^\circ$.

For a general value of θ , there are two inequivalent distances between A and equatorial Os. The shorter of these two distances is labelled r_4 in Figure 4c and the longer is labelled d_{AO} . In the limit that $\theta = 0^\circ$, $d_{AO} = r_4$ for all r_4/r_1 , and d_{AO} becomes greater than r_4 as θ increases. The corkscrew model assumes that the shorter bond is very stiff and thus r_4 remains constant, whereas the longer bond is so much longer that it has negligible stiffness and d_{AO} is unrestricted. This assumption breaks down at very low θ where $d_{AO} \approx r_4$. For a given θ , Figure 5 shows that d_{AO}/r_4 is greatest when $r_4 \approx r_1$, but as r_4/r_1 becomes greater the maximum d_{AO} differs less from r_4 . Although it is difficult to estimate the stiffness of A–O bonds for different d_{AO} distances without accurate electronic structure calculations, and therefore difficult to give a lower limit on the reasonable d_{AO}/r_4 ratio at which the model is valid, it is clear that the need for $d_{AO} \gg r_4$ places a lower limit on the range of θ and an upper limit on the range of r_4/r_1 .

Finally, in Figure 4c, the distance between A cations above and below the (001) plane containing the equatorial Os is labelled as d_{AA} . Like d_{OO} discussed previously, it is unphysical for these A cations to become arbitrarily close to one another. Figure 5 shows that in the lower limit of r_4/r_1 , d_{AA} becomes very small for low values of θ such that $d_{AA}(\theta = 0^\circ) = 0$ if $r_4 = r_1$. If we assume that an unrotated parent phase can exist, even if the corkscrew model does not apply in this parent phase, low values of θ must be structurally achievable. Consequently, there is a lower limit on the possible r_4/r_1 .

The requirements that $d_{AO} \gg r_4$ for θ at which the model applies and $d_{AA} \gg 0$ for all θ place restrictions on the lower and upper values of r_4/r_1 . Since the Ruddlesden-Popper phases being discussed are layered perovskites with frozen octahedral rotations, a realistic range of r_4/r_1 could be estimated from typical values of Goldschmidt tolerance factors, t . In perovskites with frozen octahedral rotations, $t < 1.0$ and perovskites are rarely stable with tolerance factors below $t \approx 0.85$. These restrict r_4/r_1 to the range $1.2 \leq r_4/r_1 \leq \sqrt{2}$. We have already placed an upper limit $\theta < 24^\circ$ to prevent d_{OO} becoming too small. If $r_4 = \sqrt{2}r_1$, restricting $\theta > 6^\circ$ ensures that d_{AO} is at least 10% larger than r_4 . These limits are only guesses at the values of θ and r_4/r_1 for which one expects the assumptions of the model to be violated in a real ionic material; blue

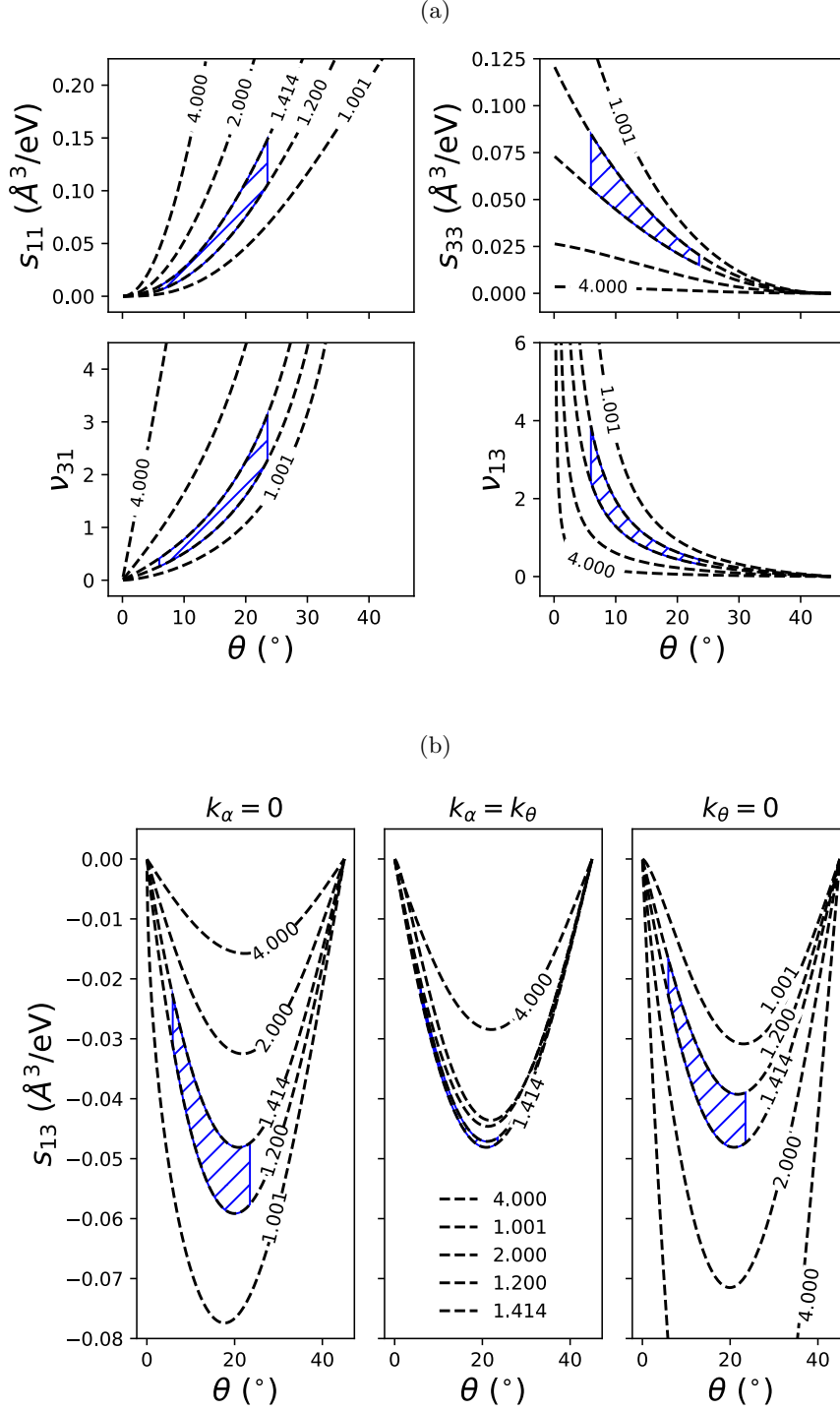


Figure 6: (a) s_{11} & s_{33} diagonal components of the compliance matrix and ν_{31} & ν_{13} Poisson's ratios and (b) s_{13} off-diagonal coupling component of the compliance matrix, all as a function of θ for different r_4/r_1 ratios. The blue hashed regions in (a) & (b) show the ranges of θ and r_4/r_1 where the mechanism may reasonably operate in a real system. In all panels in (a) $k_\theta = k_\alpha = 1$ whereas in (b) different panels show different k_α/k_θ ratios, always under the constraint that $k_\theta + k_\alpha = 2$.

hashed regions have been added to all graphs to indicate ballpark values accessible by a physically plausible system.

5 Prediction of Compliances

In order to compute compliance components, we fix that $r_1 = 1.0$ and the hinge stiffnesses in Equation (18) are also assigned arbitrary values of $k_\theta = k_\alpha = 1.0$.

Figure 6a presents the behaviour of the s_{11} and s_{33} compliance components as a function of θ for different values of r_4/r_1 . In the limit $\theta \rightarrow 0^\circ$, $s_{11} \rightarrow 0$ for all r_4/r_1 , yet s_{11} increases rapidly as θ becomes larger, with the highest r_4/r_1 corresponding to the greatest s_{11} . In contrast s_{33} shows the opposite behaviour as $s_{33} \rightarrow 0$ since $\theta \rightarrow 45^\circ$ for all r_4/r_1 and s_{33} is very large for low θ and low r_4/r_1 ; although for larger r_4/r_1 the change in s_{33} with θ is very small.

Despite the appearance of Figure 6a, s_{11} is finite for all values of θ and r_4/r_1 . This should be evident from Equation (21), since $s_{11} = 1/E_1$ and E_1 is always non-zero providing that $k_\theta, k_\alpha > 0$. Similarly, s_{33} is finite except in the limit $r_4 = r_1$ and $\theta \rightarrow 0^\circ$, since this is the only limit in which E_3 is zero. The limit $r_4 = r_1$, as well as the $\theta = 0^\circ$ and $\theta = 45^\circ$ extremes where the corkscrew model is perfectly stiff along one axis, were ruled out for a physical system in Section 4 and the blue hashed regions in Figure 6a correspond to finite and non-zero compliances. However, for both s_{11} and s_{33} , within this hashed region, the compliance is very sensitive to changes in θ . The lower two panels of Figure 6a show the Poisson ratios ν_{13} and ν_{31} . These are both positive for all θ and r_4/r_1 and thus this mechanism does not lead to auxetic behaviour coupling in-plane and layering axes. Inspecting Equations (12) and (13) we see that both ν_{13} and ν_{31} are undefined for all r_4/r_1 in the limits $\theta \rightarrow 0^\circ$ and $\theta \rightarrow 45^\circ$ respectively.

The three panels of Figure 6b show the off-diagonal compliance matrix component, s_{13} , against θ and r_4/r_1 for the cases that $(k_\theta, k_\alpha) = (2, 0)$, $(1, 1)$ and $(0, 2)$. Whereas the s_{11} (s_{33}) axial compliance increases (decreases) monotonically with θ , in both the limits $\theta = 0^\circ$ and $\theta = 45^\circ$ $s_{13} = 0$ for all r_4/r_1 , yet decreases to reach a minimum between these limits. From Equation 25, we see that $s_{13} = -\nu_{13} s_{11} = -\nu_{31} s_{33}$. Hence, $\nu_{ij} \rightarrow \infty$ in the same limit that the corresponding axial compliance $s_{ii} \rightarrow 0$ meaning that s_{13} has moderate values for all θ and r_4/r_1 and that $s_{13} \rightarrow 0$ at the limits of θ .

So far we have not discussed the effect of k_θ and k_α on the elastic compliances. In the case that $k_\alpha = 0$ (the first panel in Figure 6b), the work, W , in Equation (18) is constant for all θ and r_4/r_1 . In this case $|s_{13}|$ is maximised when $r_4 \approx r_1$, however the elastic coupling between X_1 and X_3 becomes weaker as $r_4 \gg r_1$. Since $|s_{13}|$ is greatest for $\theta \approx 20^\circ$, inspecting the blue hashed region of Figure 6b we see that the strength of compliance coupling is greatest for the largest θ within the range of potentially physical values identified previously.

If $k_\alpha > 0$, W contains a $\frac{d\alpha}{d\theta}$ term that was plotted as a function of θ and r_4/r_1 in Figure 4b. In the special case that $r_4 = \sqrt{2}r_1$, $\frac{d\alpha}{d\theta} = 1$ for all θ and therefore, since $k_\theta + k_\alpha = 2$ in every panel, W is constant and the $r_4 = \sqrt{2}r_1$ contour is unchanged between panels in Figure 6b. For contours where $r_4 \neq \sqrt{2}r_1$, increasing the k_α weighting significantly affects the s_{13} dependence upon r_4/r_1 such that in the final $(k_\theta, k_\alpha) = (0, 2)$ panel, the order of contours is flipped as compared to the first $(2, 0)$ graph. The intermediate, $(1, 1)$ case, also used to compute the axial compliances in Figure 6a, has a change in ordering of the r_4/r_1 contours yet again, with the $r_4 = \sqrt{2}r_1$ contour now corresponding to the highest $|s_{13}|$ values. Since the blue hashed region is bounded by the invariant $r_4 = \sqrt{2}r_1$ contour, the compliance components of systems with parameters in this region are only weakly dependent upon k_α/k_θ .

6 Extending to arbitrary n

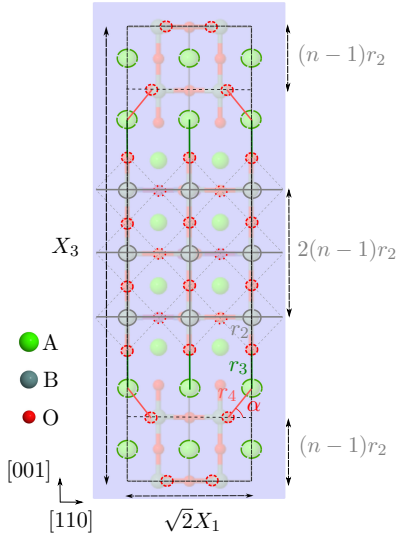


Figure 7: The cross section of the $(\bar{1}\bar{1}0)$ plane of an $n = 3$ phase with a frozen rotation about the layering axis to represent a general member of the $A_{n+1}B_nO_{3n+1}$ series. Atoms lying on the plane are shown as dashed circles and dashed squares show the outline of BO_6 octahedra. The lattice parameters X_1 – X_3 and shortest bond lengths r_1 – r_4 are labelled alongside the in-plane rotation angle, θ and the angle, α , between the A cation and the plane containing the B cation and equatorial O.

It is then straightforward to use the new definitions of X_3 and W to construct the terms of the \mathbf{s} matrix in Equation (25) as a function of any n .

$$s_{11} = s_{12} = \left(\frac{\sin^2(\theta)}{4} \right) \frac{r_1^2 X_3}{\left[n k_\theta + k_\alpha \left(\frac{d\alpha}{d\theta} \right)^2 \right]}, \quad (29)$$

$$s_{33} = \left(\frac{\cos^2(\theta) [\sin(\theta) + \cos(\theta)]^2}{\tan^2(\alpha)} \right) \frac{r_1^4}{X_3 \left[n k_\theta + k_\alpha \left(\frac{d\alpha}{d\theta} \right)^2 \right]}, \quad (30)$$

$$s_{13} = - \left(\frac{\sin(2\theta) [\sin(\theta) + \cos(\theta)]}{4 \tan(\alpha)} \right) \frac{r_1^3}{\left[n k_\theta + k_\alpha \left(\frac{d\alpha}{d\theta} \right)^2 \right]}. \quad (31)$$

Inspecting Equation (27), we see that it has the form $X_3 = an + b$ where b contains the component to X_3 that may change with changing θ and that this term forms a smaller proportion of X_3 as n increases. It was shown previously that the behaviour of W with changing θ is weakly dependent upon k_α/k_θ when $r_4/r_1 \neq \sqrt{2}$. On the other hand, Equation (28) shows that when comparing structures with different n , the k_α/k_θ ratio is extremely important such that if $k_\alpha/k_\theta \ll 1$, $W \propto n$ whereas if $k_\alpha/k_\theta \gg 1$, $W \propto 1$. Using this insight, in Table 1 we show the dependence of s_{11} , s_{33} and s_{13} on n for different k_α/k_θ regimes.

The derivation in Section 2 focused only on the $n = 1$ member of the $A_{n+1}B_nO_{3n+1}$ series, however it is possible to extend this derivation to a system of general layer thickness n . Figure 7 shows the $(\bar{1}\bar{1}0)$ plane of the $Acam$ phase of $n = 3$ $A_4B_3O_{10}$, the same plane displayed in Figure 2c for $n = 1$ A_2BO_4 .

The in-plane structure (i.e. the cross section through the (001) and (002) planes shown in Figure 2b) is exactly the same in the $n = 3$ and $n = 1$ cases. Therefore for $n = 3$, X_1 and X_2 will be given by Equation (2) and hence $\nu_{12} = -1$ also.

Additional planes of BO_6 octahedra clearly affect the expression for X_3 , however. Noting that the thickness of the cell edge and middle perovskite layer blocks have both increased by $n - 1$ BO_6 units (each $2r_2$ in height) between Figure 2c and Figure 7, but the same number of r_3 and r_4 bonds remain. We may express X_3 generally as:

$$X_3 = 2[(2n - 1)r_2 + r_3 + r_4 \sin(\alpha)] \quad (27)$$

Similarly, since each BO_6 layer contains 4 θ -hinges, there are n BO_6 layers per perovskite block and 2 perovskite blocks in the unit cell, Equation (18) may be generalised:

$$W = 16 \left[n k_\theta + k_\alpha \left(\frac{d\alpha}{d\theta} \right)^2 \right] (d\theta)^2 \quad (28)$$

$$\begin{array}{llll}
k_\alpha/k_\theta \ll 1 & s_{11} \propto 1 + \frac{c}{n} & s_{33} \propto \frac{1}{n(n+c)} & s_{13} \propto -\frac{1}{n} \\
k_\alpha/k_\theta \gg 1 & s_{11} \propto n + c & s_{33} \propto \frac{1}{n+c} & s_{13} \propto 1
\end{array}$$

Table 1: Proportionality of various components of the elastic compliance matrix s_{ij} to the perovskite layer thickness n for different regimes in the ratio of harmonic hinge stiffnesses related to the α and θ bond angles.

Since $n \geq 1$, there is no problem if any of the compliances cease to make sense in the limit $n \rightarrow 0$. However, pure ABO_3 perovskite represents the $n = \infty$ limit of the RP series and therefore the compliances in this limit should have a physical interpretation. The only term in Table 1 that looks problematic as $n \rightarrow \infty$ is $s_{11} \propto n + c$ under the condition $k_\alpha/k_\theta \gg 1$. It should be noted in this case that providing $k_\theta > 0$ and k_α is finite, there will be a sufficiently high n for which $n k_\theta \gg k_\alpha$ and thus $s_{11} \propto 1$ behaviour is recovered ($\frac{c}{n}$ is vanishingly small in this limit). Only in the case that $k_\theta = 0$, would $n = \infty$ represent a system with no resistance to changing θ and therefore have infinite in-plane compliance. Providing $k_\theta > 0$ and k_α is finite, all compliances behave as $k_\alpha/k_\theta \ll 1$ when $n \gg 1$ and therefore in the limit $n \rightarrow \infty$, the in-plane compliance s_{11} tends to a constant value whereas both axial compliance s_{33} and elastic coupling between the 1 and 3 axes s_{13} tend to 0 for all k_α/k_θ .

7 Conclusions

For a tetragonal A_2BO_4 Ruddlesden–Popper structure with a frozen octahedral rotation about the layering axis, we assumed that the four shortest metal–anion bonds are so stiff compared to other interatomic interactions that these bonds remain perfectly rigid. This assumption leaves only a single internal degree of structural freedom, the rotation angle, θ , which is directly coupled to the in-plane and axial lattice parameters. For this model, the previously proposed “corkscrew” mechanism, we formulated equations relating structural parameters to θ and the bond lengths of the four fixed bonds. Analysing these equations allowed us to identify the structural limitations of the model and considering the parameter values at which the assumptions of the model might break down allowed us to identify a “physically relevant” region of the parameter space. Assuming that the only resistance to deformation comes from resistance to change in bond angles, we were further able to derive equations for components of the elastic compliance matrix and investigate how these compliances behave with changes in θ , the ratios of fixed bond lengths and the relative strengths of the harmonic potentials on the bond angles. Finally, we extended this model for the $n = 1$ member of the $\text{A}_{n+1}\text{B}_n\text{O}_{3n+1}$ series to a general n and discussed how different compliance components change with n . Although this idealised model is unlikely to quantitatively represent any real chemical system, analysing the corkscrew mechanism in this limit might help understand real systems where the mechanism operates in addition to other physical effects.

8 Acknowledgements

CA is supported by a studentship in the Centre for Doctoral Training on Theory and Simulation of Materials at Imperial College London funded by the EPSRC (EP/L015579/1). This work was supported by the Thomas Young Centre under grant TYC-101. CA acknowledges support from the Armourers and Brasiers Gauntlet Trust for a research studentship travel grant. MS acknowledges the Royal Society for a fellowship.

References

- [1] M. S. Senn, A. Bombardi, C. A. Murray, C. Vecchini, A. Scherillo, X. Lui, and S. W. Cheong. Negative thermal expansion in hybrid improper ferroelectric ruddlesden–popper perovskites by symmetry trapping. *Phys. Rev. Lett.*, 114:035701, 2015.

- [2] Junichi Takahashi and Naoki Kamegashira. X-ray structural study of calcium manganese oxide by rietveld analysis at high temperatures. *MRS Bulletin*, 28(6):565 – 573, 1993.
- [3] Chris Ablitt, Sarah Craddock, Mark S. Senn, Arash A. Mostofi, and Nicholas C. Bristowe. The origin of uniaxial negative thermal expansion in layered perovskites. *npj Computational Materials*, 3(1):44, 2017.
- [4] Q. Huang, J. L. Soubeyroux, O. Chmaissem, I. Natali Sora, A. Santoro, R. J. Cava, J. J. Krajewski, and W. F. Peck Jr. Neutron powder diffraction study of the crystal structures of Sr₂RuO₄ and Sr₂IrO₄ at room temperature and at 10 k. *J. Solid State Chem.*, 112:355–361, 1994.
- [5] T. Vogt and D.J. Buttrey. Temperature dependent structural behavior of Sr₂RhO₄. *J. Solid State Chem.*, 123(1):186 – 189, 1996.
- [6] Ben Ranjbar and Brendan J. Kennedy. Anisotropic thermal expansion in Sr₂RhO₄ - a variable temperature synchrotron x-ray diffraction study. *Solid State Sciences*, 49:43 – 46, 2015.
- [7] M. T. Dove, V. Heine, and K. D Hammond. Rigid unit modes in framework silicates. *Min. Mag.*, 59:629–639, 1995.
- [8] M. T. Dove, K. O. Trachenko, M. G. Tucker, and D. A. Keen. Rigid unit modes in framework structures: Theory, experiment and applications. *Rev. Mineral. Geochem.*, 39:1, 2000.
- [9] Mark S. Senn, Claire A. Murray, Xuan Luo, Lihai Wang, Fei-Ting Huang, Sang-Wook Cheong, Alessandro Bombardi, Chris Ablitt, Arash A. Mostofi, and Nicholas C. Bristowe. Symmetry switching of negative thermal expansion by chemical control. *J. Am. Chem. Soc.*, 138(17):5479, 2016.
- [10] E. Grüneisen and E. Goens. Thermal expansion of zinc and cadmium. *Z. Phys.*, 29:141, 1924.
- [11] T. H. K. Barron and R. W. Munn. Analysis of the thermal expansion of anisotropic solids: Application to zinc. *Philosophical Magazine*, 15(133):85, 1967.
- [12] H. Fang, M. T. Dove, and K. Refson. Ag–Ag dispersive interaction and physical properties of Ag₃Co(CN)₆. *Phys. Rev. B*, 90:054302, 2014.
- [13] C.W Smith, J.N Grima, and K.E Evans. A novel mechanism for generating auxetic behaviour in reticulated foams: missing rib foam model. *Acta Materialia*, 48(17):4349 – 4356, 2000.
- [14] Joseph N. Grima, Elaine Chetcuti, Elaine Manicaro, Daphne Attard, Matthew Camilleri, Ruben Gatt, and Kenneth E. Evans. On the auxetic properties of generic rotating rigid triangles. *Proceedings of the Royal Society of London A: Mathematical, Physical and Engineering Sciences*, 2011.
- [15] Daphne Attard and Joseph N. Grima. Auxetic behaviour from rotating rhombi. *physica status solidi (b)*, 245(11):2395–2404, 2008.
- [16] Joseph N. Grima, Elaine Manicaro, and Daphne Attard. Auxetic behaviour from connected different-sized squares and rectangles. *Proceedings of the Royal Society of London A: Mathematical, Physical and Engineering Sciences*, 2010.
- [17] Joseph N. Grima, Roberto Caruana-Gauci, Daphne Attard, and Ruben Gatt. Three-dimensional cellular structures with negative poisson’s ratio and negative compressibility properties. *Proceedings of the Royal Society of London A: Mathematical, Physical and Engineering Sciences*, 2012.
- [18] Chris Ablitt, A. Mostofi, Arash, C. Bristowe, Nicholas, and S. Senn, Mark. Control of uniaxial negative thermal expansion in layered perovskites by tuning layer thickness. *Front. Chem.*, 2018.

- [19] J. N. Grima and K. E. Evans. Auxetic behavior from rotating squares. *Journal of Materials Science Letters*, 19(17):1563–1565, Sep 2000.